Redox Electrochemistry of Mn(II) via Carbon Black Nanoparticle Impacts

Keal, Molly; Courtney, James; Rees, Neil

DOI:
10.1021/acs.jpcc.3c02964

Document Version
Publisher's PDF, also known as Version of record

Citation for published version (Harvard):
Keal, M, Courtney, J & Rees, N 2023, 'Redox Electrochemistry of Mn(II) via Carbon Black Nanoparticle Impacts', *Journal of Physical Chemistry C*, vol. 127, no. 27, pp. 13380-13388. https://doi.org/10.1021/acs.jpcc.3c02964

THE JOURNAL OF PHYSICAL CHEMISTRY C
A JOURNAL OF THE AMERICAN CHEMICAL SOCIETY

pubs.acs.org/JPCC

Article

Redox Electrochemistry of Mn(II) via Carbon Black Nanoparticle Impacts

Molly E. Keal, James M. Courtney, and Neil V. Rees*

Cite This: https://doi.org/10.1021/acs.jpcc.3c02964

Read Online

ACCESS | Metrics & More | Article Recommendations | Supporting Information

ABSTRACT: The field of impact electrochemistry, namely, electrochemical processes occurring at nanoparticles during collisions with a substrate electrode, has recently been applied to the recovery of commercially important metals. In this study, the reduction and oxidation of solution Mn(II) were observed on carbon black particles during nanoimpacts, with the onset potentials of the reduction and oxidation processes in good agreement with solution voltammetry. The formation of Mn(0) and MnO_2 was confirmed via scanning electron microscopy/energy-dispersive X-ray (SEM/EDX) analysis and X-ray photoelectron spectroscopy (XPS) analysis. Coverages of between 0.2 and 0.6 monolayer equivalents were obtained for the reductive deposition of Mn, whereas for the anodic deposition of MnO_2, a more complex picture was found due to the oxidation pathway from Mn(II) to MnO_2.

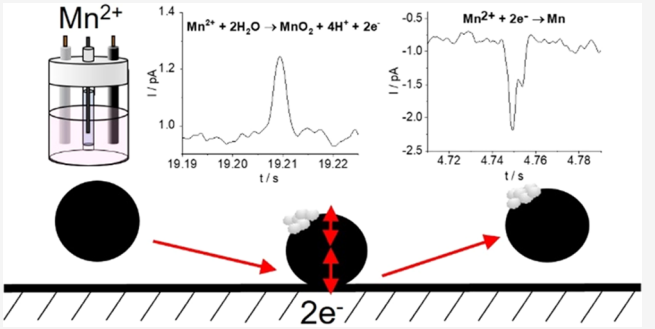

INTRODUCTION

The recovery of commercially important metals from waste and/or recycling streams is imperative for their sustainable use as well as minimizing harmful environmental and health hazards associated with disposal. Current recovery methods such as ion exchange,[1] chemical precipitation,[2] and adsorption/biosorption are generally not economically viable for low concentrations of such metals as they involve costly preconcentration and separation steps.[3] These processes are energy-intensive, involve consumption of considerable amounts of reagent, and can generate secondary pollutants.[4,5]

Electrochemical techniques would appear well-suited to metal recovery, with methods such as electrowinning and electrodeposition boasting selective metal recovery in high purity with a reduced solvent and energy consumption compared to metallurgical methods.[6,7] However, these techniques usually require a high aqueous metal ion concentration at the industrial scale which is not often the case in waste effluent streams where there are trace concentrations of commonly found heavy metals.[8]

Using nanoimpact electrochemistry to recover metal species has numerous advantages compared to other electrochemical methods in that it has a high rate of mass transport to the nanoparticles and lessens the fouling of a single electrode by providing high numbers of particles onto which the target metal can be electroreduced.[9] This technique involves the introduction of nanoparticles into the solution (containing an inert supporting electrolyte and analyte), which then move under Brownian motion and can randomly collide with the electrode;[10−14] although convection can be applied if required.[15−17] When the working electrode is held at a suitable potential, the particles themselves can either be reduced or oxidized or upon collision the nanoparticles can provide a surface where the oxidation/reduction of a species in solution can take place.[10] It is this latter impact experiment that is relevant to metal deposition, where metal ions in solution can be reduced onto the impacting nanoparticle during the collision. Here, we assume that during impacts, the metal is reduced onto the particle itself; however, when the working electrode and particles are the same material (e.g., carbon), competition can occur between these two materials, and there is a possibility of metal ions being reduced/oxidized on the electrode surface during "impact". Analysis of the resulting transient signals can determine a range of information including nanoparticle size, concentration, and charge transfer kinetics of a system.[18−29] In the context of metal recovery, there are few reports concerning the electrodeposition of metals using nanoimpact electrochemistry, and until recently, these were limited to metal nanoparticle cores only.[30−32] More recently, the electrodeposition of copper onto fly-ash cenospheres and palladium on carbon black has been reported as well as the rapid screening of bimetallic catalysts.[9,33,34]

Received: May 5, 2023
Revised: June 5, 2023

Manganese is a commercially significant metal used in applications such as batteries and steelmaking.[35,36] If manganese is left untreated in wastewater, it can cause detrimental health effects, in severe cases leading to "manganism" affecting the central nervous system.[36,37] Current recovery methods of manganese from battery waste rely on metallurgical techniques[38,39] following an initial physical separation step:[40] a technique such as nanoimpact electrochemistry may be advantageous in terms of efficiency, as it can simplify the recovery process.[33] The bulk electrodeposition of Mn has been well-studied in the literature, primarily in sulfate and chloride solutions.[41−43] Despite the higher current efficiency observed when using chloride baths, it is conventionally produced from manganese(II) sulfate/ammonium sulfate solutions to avoid the formation of Cl_2 gas and due to the corrosive nature of the solution.[44] Ammonium sulfate acts as both an electrolyte and buffer in these solutions,[44] and it has been speculated that it prevents the formation of insoluble manganese hydroxides during electrodeposition by promoting the formation of soluble ammonium complexes.[45,46] However, chemical analysis of manganese deposited in the presence of $(NH_4)_2SO_4$ still results in the presence of oxides and hydroxides.[47,48]

Another commonly used additive is selenium dioxide which has been shown to inhibit the hydrogen evolution reaction (HER) through the reduction of Se(IV) to Se(0) on the electrode surface, altering its morphology and electrochemical properties such that the HER overpotential was increased.[49,50] However, in addition to the toxic nature of SeO_2, it also results in contamination of the manganese deposits, and precipitation of these compounds in the electrolyte can prove problematic.[51] Organic additives such as carboxylic acids and polyacrylamide have also been tested to improve the crystallinity of deposits with limited success.[52]

In order to determine whether the nanoimpact method may be a candidate for the recovery of aqueous Mn(II), this study investigates the deposition of oxidation and reduction products (MnO_2 and Mn) from manganese(II) sulfate solution at neutral pH on carbon black particles (CB, nominal diameter 50 nm) without the use of any additives. Scaled-up deposition experiments were conducted to generate sufficient deposited materials for characterization, and the reduction product was confirmed by X-ray photoelectron spectroscopy (XPS) to Ru(0) on CB, and the product of the oxidative impacts was found to be predominantly α-MnO_2 and MnOOH on CB by Raman spectroscopy and XPS. The oxidative deposition products are found to reflect the complex mechanism of the formation of MnO_2.

EXPERIMENTAL SECTION

The following chemicals were purchased and used without further purification: manganese(II) sulfate monohydrate (99%, Sigma-Aldrich), potassium sulfate (99%, Sigma-Aldrich), and Vulcan XC 72R carbon black (Fuel Cell Store). All solutions were made using ultrapure water (with a resistivity ≥18.2 MΩ·cm). Solutions were thoroughly degassed using nitrogen (oxygen-free, BOC Gases plc), and a nitrogen atmosphere was maintained throughout experiments.

A three-electrode cell arrangement was used for all electrochemical experiments consisting of a standard calomel electrode (SCE, saturated with KCl) as the reference electrode, a graphite rod (5 mm, Goodfellow Cambridge Ltd.) as the counter electrode, and either a carbon fiber microelectrode (diameters: 9, 33 μm, and array) or a glassy carbon (diameter: 3 mm) macroelectrode as the working electrode. The 9 μm and array working electrodes were made in-house using pitch-derived carbon fiber (Goodfellow Cambridge Ltd.), while the 33 μm carbon fiber electrode was purchased from IJ Cambria Ltd. The glassy carbon (GC) electrode was made in-house using glassy carbon rod purchased from Alfa Aesar. All of the working electrodes were prepared by polishing on microcloth pads with alumina suspensions of 1, 0.3, and 0.05 μm sequentially (all from Buehler Inc.). Unless otherwise stated, the reaction solution consisted of 0.5 mM $MnSO_4$ and 20 mM K_2SO_4. All standard electrochemical experiments were conducted using an Autolab 128 N potentiostat (Metrohm-Autolab BV, Netherlands) controlled by a PC with Nova 2.1 software.

For impact experiments, the solution had carbon black nanoparticles (number concentration of 5 pM) added to it. The carbon black (CB) suspension was sonicated for 30 min before use. Chronoamperograms (duration of 30 s) were conducted using the same three-electrode cell as described previously in a bespoke low-noise potentiostat controlled by a PC with PyFemto software.[9] Impact electrochemical data were analyzed following electronic filtration (digital) at 250 Hz to improve the signal-to-noise ratio and facilitate analysis. Impact spikes were analyzed by using OriginPro 2021 software for spike identification and integration: the baseline was set using the filtered data in short time sections, and the peak search was automated based on a threshold criterion that the spike height should be at least 80% of the that of the largest spike signal, in order to give confidence that random noise signals were not counted.

Long-term impact experiments were performed in the solution stated above with the addition of higher-concentration carbon black nanoparticles (500 pM). The three-electrode cell used consisted of a saturated SCE reference electrode in a separate fritted compartment, graphite plate electrode (diameter: 2.5 cm) as the working electrode, and graphite rods (Alfa Aesar) as the counter electrode. The post-chronoamperometric solution was filtered and washed under vacuum using Anodisc 47 filter paper with a pore size of 0.02 μm and a diameter of 47 mm, and the resulting filter cake was dried at 40 °C. For the XPS characterization, the samples were analyzed (at NMRC, University of Nottingham) using a Kratos Liquid Phase Photoelectron Spectrometer (LiPPS, in dry sample mode) with monochromated Al Kα X-ray source (1486.6 eV) operated at 10 mA emission current and 12 kV anode potential (120 W). Data processing was conducted using CASAXPS software (version 2.3.20) for Shirley background subtraction, and peak deconvolution was conducted using a Voigt lineshape function on OriginPro 2021.

For scanning electron microscopy/energy-dispersive X-ray (SEM/EDX) analysis, GC tips were removed post-chronoamperometric scan from the plating solution, attached to carbon tape, and examined using a Hitachi TM3030 Plus electron microscope. For Raman spectroscopy analysis, a Renishaw inVia microscope with a 532 nm laser was used. All data were processed using a combination of Microsoft Excel and OriginPro 2021.

RESULTS AND DISCUSSION

To study the electrodeposition of manganese on carbon, cyclic voltammetry studies were conducted using a 33 μm carbon fiber working electrode. An onset potential has been defined as

https://doi.org/10.1021/acs.jpcc.3c02964
J. Phys. Chem. C XXXX, XXX, XXX−XXX

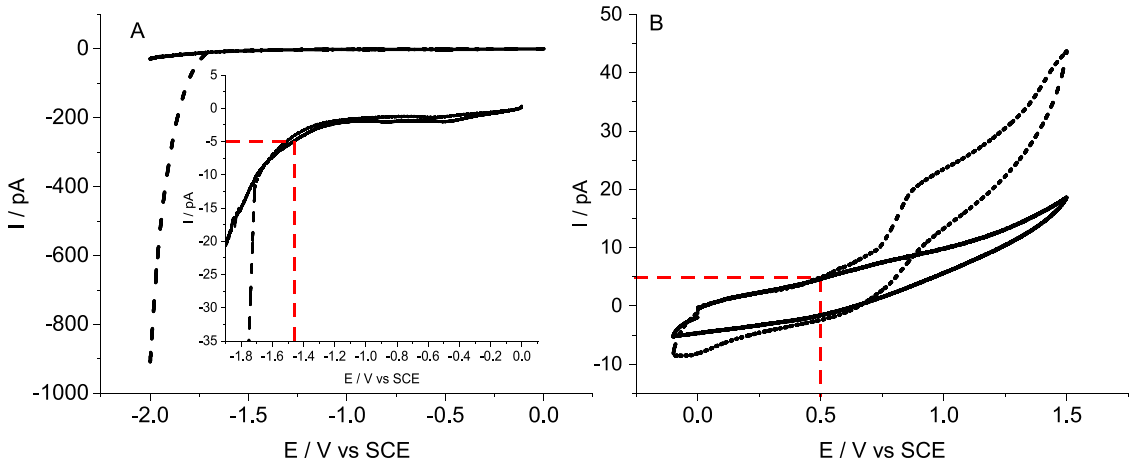

Figure 1. Cyclic voltammograms (—, solid black line) conducted in 20 mM K_2SO_4 and (--, dashed black lines) conducted in 20 mM K_2SO_4 and 0.5 mM $MnSO_4$, respectively, for (A) reductive scans and (B) oxidative scans. Both CVs were recorded using a bare 33 μm carbon fiber working electrode at a scan rate of 100 mV s^{-1}. A dashed red line (--, dashed red lines) is used to indicate the onset potential at ±5.0 pA.

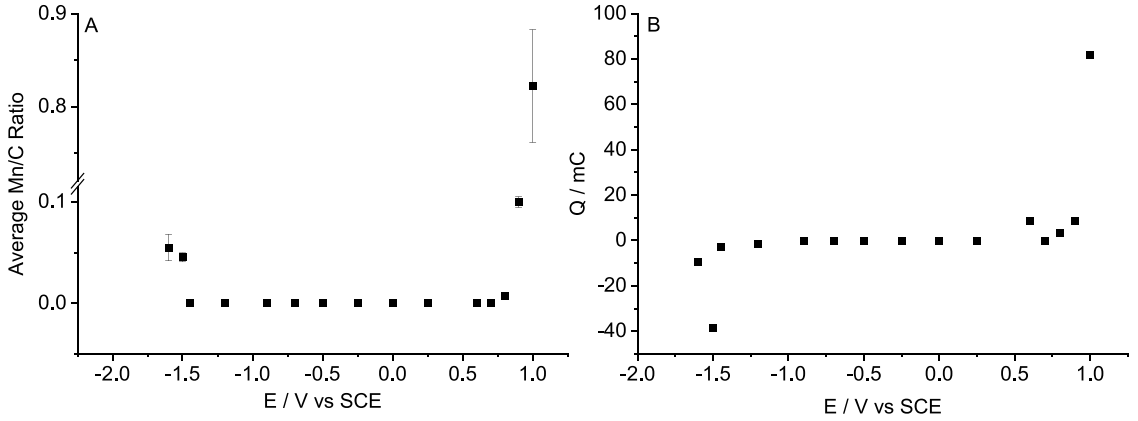

Figure 2. Graphs showing (A) the average Mn/CB ratio based on weight percent obtained via SEM/ EDX analysis at 2000× for GC tips removed from the post-chronoamperometric solution (containing 10 mM $MnSO_4$ and 20 mM K_2SO_4) across various potentials and (B) the integrated charge (Q/mC) from the respective chronoamperograms.

a sufficiently negative or positive potential to generate a current response,[9] although it can be a controversial parameter due to the range of ways in which it can be defined, many of which are (semi)arbitrary and occasionally have limited physical meaning.[53] In this case, a current of ±5.0 pA has been used to define the onset potential, based on the observed faradaic currents in both the cathodic and anodic processes (see Figure 1). First, a cyclic voltammogram (CV) was recorded in a solution of 20 mM K_2SO_4 at a voltage scan rate of 100 mV s^{-1}, scanning negatively (cathodically) from 0 V (vs SCE) as a control experiment (see Figure 1A). Then, the CV was repeated in a solution containing 0.5 mM $MnSO_4$ and 20 mM K_2SO_4, and the reduction of Mn(II) was observed (see eq 1) with an onset potential of −1.44 V (vs SCE) as shown in Figure 1A and in good agreement with the literature.[44]

$$Mn^{2+} + 2e^- \rightarrow Mn \quad (1)$$

Next, the electrode was thoroughly polished and then scanned in the same degassed solution in the positive (anodic) direction. An oxidative process was observed, and Figure 1B shows the result of these CV scans in 20 mM K_2SO_4 and 0.5 mM $MnSO_4$/20 mM K_2SO_4 solutions at a scan rate of 100 mV s^{-1}. The onset potential of the oxidation, according to the previous definition, was observed at +0.48 V (vs SCE) in good agreement with the literature[54] corresponding to the oxidation of $Mn^{2+}(aq)$ to produce MnO_2, as illustrated in the overall eq 2 below.[55] However, it has been reported that it is unlikely to occur directly and instead occurs via a multistep reaction. The first step in this mechanism is the oxidation of adsorbed Mn^{2+} ions on the electrode surface to Mn^{3+} (eq 3), followed by either disproportionation to produce Mn^{2+} and Mn^{4+} (eq 4) or hydrolysis to produce an intermediate MnOOH (eq 6) depending on the stability of the Mn^{3+} ion in solution. At pH 7, Mn^{3+} is shown to be thermodynamically unstable with respect to disproportionation (see Section A of the Supporting Information for calculations). Equations 5 and 7 involving the precipitation of MnO_2 are reported to be kinetically slow.[55−60]

$$Mn^{2+}(aq) + 2H_2O(l) \rightarrow MnO_2(s) + 4H^+(aq) + 2e^- \quad (2)$$

$$Mn^{2+}(ads) \rightarrow Mn^{3+}(aq) + e^- \quad (3)$$

Disproportionation pathway

$$2Mn^{3+}(aq) \rightarrow Mn^{2+}(aq) + Mn^{4+}(aq) \quad (4)$$

$$Mn^{4+}(aq) + 2H_2O(l) \rightarrow MnO_2(s) + 4H^+(aq) \quad (5)$$

Hydrolysis pathway

https://doi.org/10.1021/acs.jpcc.3c02964
J. Phys. Chem. C XXXX, XXX, XXX−XXX

$$Mn^{3+}(aq) + 2H_2O\ (l) \rightarrow MnOOH(s) + 3H^+(aq) \quad (6)$$

$$MnOOH(s) \rightarrow MnO_2(s) + H^+(aq) + e^- \quad (7)$$

The electrodeposition of manganese and manganese dioxide on carbon working electrodes was further investigated using SEM/EDX analysis to establish a potential window to use in the impact electrochemistry experiments. A chronoamperometric experiment was conducted in a degassed solution containing 20 mM potassium sulfate and 10 mM manganese sulfate for 5 min at various potentials between −1.6 and +1.0 V (vs SCE). The tip of the GC working electrode was then analyzed using SEM/EDX. Figure 2A shows the average manganese-to-carbon ratio obtained using EDX analysis at a magnification of 2000×. Significant levels of manganese were observed at overpotentials negative of −1.45 V (vs SCE), consistent with the onset potential for Mn(II) reduction. Significant levels of manganese were also observed at overpotentials positive of +0.8 V (vs SCE). A small amount of manganese was observed at potentials between +0.5 and +0.8 V (vs SCE), which is consistent with the onset potential for Mn(II) oxidation as previously stated. The resulting charge from integration of the chronoamperograms is shown in Figure 2B. SEM images of the GC electrodes were obtained at a magnification of 2000× at these two potentials, showing a needle-type structure for the electrode held at −1.6 V vs SCE and a continuous film with some defects for the electrode held at 1.0 V vs SCE (See Section B of the Supporting Information).

NANOIMPACT EXPERIMENTS

To determine whether impacts could be detected due to manganese reduction and oxidation processes, chronoamperometry was conducted with and without the addition of carbon black (5 pM) in a solution containing 0.5 mM $MnSO_4$ and 20 mM K_2SO_4 at a series of potentials from +0.9 to −1.6 V (vs SCE). Impact experiments were performed at potentials from −1.4 to −1.6 V (vs SCE) to observe the reduction process (eq 1). Impacts were observed with an onset potential of −1.45 ± 0.01 V (vs SCE), in good agreement with Figure 1, and a plot of the charge passed (Q/fC) is given in Figure 3 along with a typical chronoamperogram. It is noted that a variety of spike forms are present from single sharp features to larger "step on, step off"-type signals, indicating a range of impact durations and particle−electrode interactions[33,61] as shown in Figure 3A. Figure 3B shows the variation in charge passed per impact with potential and the onset potential of ca. −1.45 V (vs SCE). The apparent trend of the lowering in mean charge passed per impact as overpotential increases is due to some data points skewing the mean—hence the large overlapping error bars. Impact experiments are often subject to significant variation due to the multiple factors that contribute to the range of charges measured at each potential, such as the number of measurements, the size of impacting particle (single vs aggregated), the shape of the impact signal (sharp single spikes vs "bursts" of spikes vs step on−step off spikes), and other reactions that may occur on the particles at those potentials (e.g., hydrogen evolution etc.).

The calculated coverage (Figure 3C) at all potentials was found to be less than monolayer (see the SI for calculations), indicating slow kinetics for manganese reduction.

Analogous impact experiments were conducted between +0.40 and +0.90 V vs SCE to investigate the oxidation of

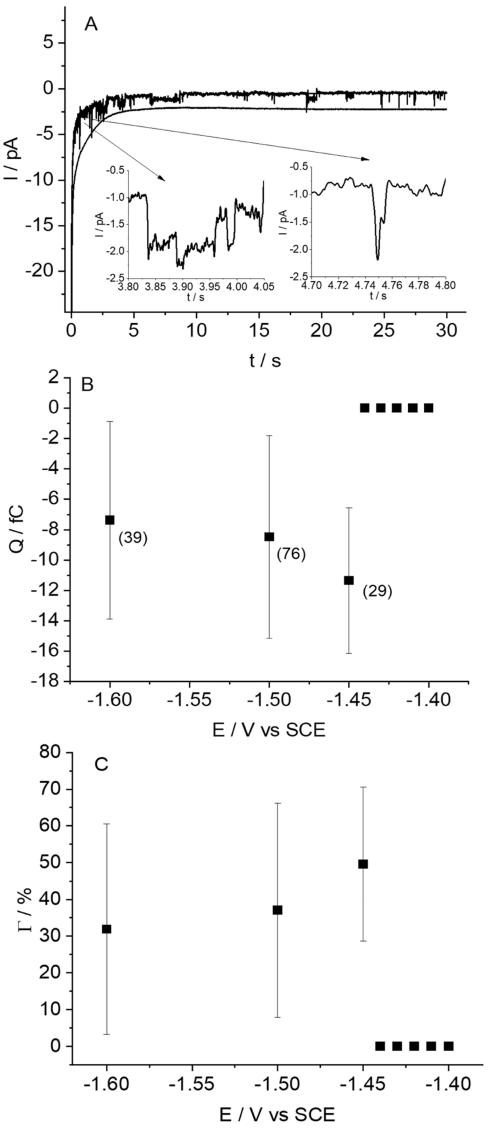

Figure 3. (A) Representative 30 s chronoamperogram conducted in a solution containing 0.5 mM $MnSO_4$ and 20 mM K_2SO_4 solution with a 9 μm CF electrode held at −1.6 V vs SCE before (i) and after (ii) the addition of 5 pM carbon black nanoparticles with an inset example of two zoomed in different impacts indicating different particle−electrode interactions. (B) Integrated charge (Q/fC) from impact events from −1.4 to −1.6 V vs SCE with bracketed numbers indicating the number of impacts analyzed at the respective potential. (C) Calculated coverage of manganese on carbon black.

Mn(II), and these results are shown in Figure 4. The onset of oxidative spikes was observed at +0.50 ± 0.01 V (vs SCE) also in good agreement with Figure 1. An example of a typical chronoamperogram is shown in Figure 4A, along with the integrated average charges of the oxidative impacts (Figure 4B).

To obtain direct evidence of Mn deposition on the carbon black nanoparticles, the experiment was scaled up to a 500 mL cell and a 5 h chronoamperogram was recorded at a potential of −1.60 V vs SCE, as this provided a significant overpotential compared to the onset potential of −1.44 V (vs SCE). A three-electrode cell consisting of a saturated SCE (KCl) as the reference electrode encased in a separate fritted compartment, a graphite plate as the working electrode, and graphite rod as the counter electrode was used in a solution containing 20 mM

https://doi.org/10.1021/acs.jpcc.3c02964
J. Phys. Chem. C XXXX, XXX, XXX−XXX

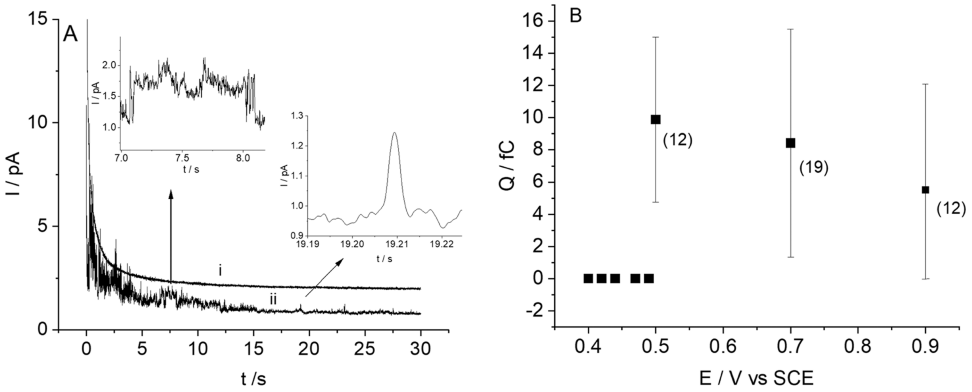

Figure 4. (A) Representative 30 s chronoamperogram conducted in a solution containing 0.5 mM $MnSO_4$ and 20 mM K_2SO_4 with a 9 μm CF electrode held at +0.90 V vs SCE before (i) and after (ii) the addition of 5 pM carbon black nanoparticles with an inset of different zoomed in impact events. (B) Integrated charge (Q/fC) from impact events ranging from a potential of +0.40 to +0.90 V vs SCE with bracketed numbers indicating the number of impacts analyzed at the respective potential.

K_2SO_4 and 0.5 mM $MnSO_4$ with the addition of 500 pM carbon black nanoparticles. The reaction solution was thoroughly deoxygenated and kept under constant agitation with nitrogen gas to maintain an oxygen-free solution, prevent sedimentation of the carbon black suspension, and increase the number of impact events. After the experiment, the solution was filtered and dried at 40 °C to yield the modified carbon black particles, which were analyzed using SEM/EDX, which revealed the presence of deposited manganese in an average carbon to manganese-to-carbon weight percent ratio of 0.030 ± 0.007 as displayed in Table 1 (for further EDX spectra and SEM images see Section C of the Supporting Information).

Table 1. Manganese Content for Unmodified CB Nanoparticles, the Sample Held at −1.6, +0.5, and +0.7 V vs SCE during Chronoamperometry[a]

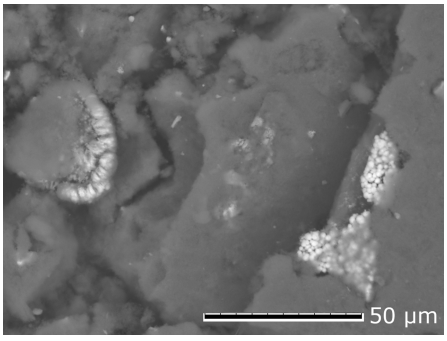

CB NP samples	SEM/EDX average weight% ratio Mn/CB
unmodified	0
−1.6 V vs SCE	0.0300 ± 0.0070
+0.5 V vs SCE	0.0200 ± 0.0070
+0.7 V vs SCE	0.0003 ± 0.0002

[a]Picture shows an SEM image of Mn/CB deposited at +0.5 V vs SCE.

The upscaled experiment was repeated for the manganese oxidation process using potentials of +0.50 V (onset of oxidative spikes) and +0.70 V vs SCE. Following the filtration of the solution, the SEM/EDX analysis of the resulting carbon black powder surprisingly revealed manganese deposited at +0.50 V with only trace detected at +0.70 V (see Table 1). We postulate that this is due to the complex nonequilibrium pathways of MnO_x formation on the nanoscale,[62−67] which often involve metastable states such as α-,β-,γ-MnOOH. Density functional theory (DFT) calculations reported by Ceder et al.[64] suggest that the above oxidizing potentials of +0.50 and +0.70 V (vs SCE) would correspond to metastable states of β-MnOOH and γ-MnOOH/MnO_2 (rutile), respectively. The picture is further complicated by the stability of the states being dependent on size (surface energy) as well as pH and potential,[64] which suggest that MnOOH and MnO_2 species may not be stable below several nanometers. We conclude that the significant decrease in the amount of Mn detected from impacts recorded at +0.5 to +0.7 V (vs SCE) indicates the interplay between the kinetics of the Mn(II) oxidation, with the relative stability of the metastable oxyhydroxide and oxide species as nucleating nanoclusters at the two potentials.

At very low overpotentials (i.e., close to the onset potential for observation of current spike signals), a black deposit was observed on the graphite electrode surface, which was confirmed to contain manganese and oxygen via SEM/EDX (see Section C of the Supporting Information), suggesting that deposition of MnO_x had preferentially occurred on the substrate electrode.

Raman spectroscopy was used to provide evidence on the identity of the MnO_x species due to its use in characterizing manganese oxides.[68−73] The Raman spectrum of the substrate electrode surface (Figure 5) exhibited 4 strong bands at 138, 501, 575, and 654 cm^{-1} as well as weaker bands at 301, 746, and 610 cm^{-1} and a broad feature at 187 cm^{-1}. No peaks were present in the spectrum of the unmodified graphite plate electrode (see Figure 5) in the chosen range (100−1000 cm^{-1}), indicating that the peaks were due to an electrodeposited manganese species and not due to the graphite electrode.

Table 2 shows the tabulated Raman signals of the recorded spectrum (Figure 5) compared to literature values for shifts corresponding to that of α, β, and γ forms of MnO_2.[69,71−73] The recorded Raman spectrum exhibits all of the peaks reported in literature corresponding to α-MnO_2 (187, 387, 577, and 654 cm^{-1}). The latter two bands (577 and 654 cm^{-1}) correspond to the two symmetric vibrations of Mn−O characteristic of α-MnO_2.[69] The sharp band exhibited at 387 cm^{-1} is due to the Mn−O bending vibration.[71,72] It is reported that the formation of the crystal phase of MnO_2 is largely dictated by the potassium concentration; the α-MnO_2 (2 × 2)

https://doi.org/10.1021/acs.jpcc.3c02964
J. Phys. Chem. C XXXX, XXX, XXX−XXX

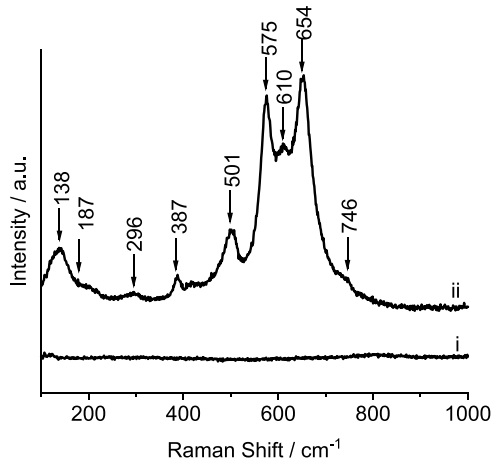

Figure 5. Raman spectrum of (i) the unmodified graphite plate electrode and (ii) the graphite plate electrode with electrodeposited Mn species.

Table 2. Raman Shift Values Obtained from the Spectrum in Figure 4 Compared to Literature Values for α-MnO_2, β-MnO_2, γ-MnO_2, and MnOOH[a]

Experimental Raman shift/ cm^{-1}	α-MnO_2 Raman shift/ cm^{-1}			β-MnO_2 Raman shift/ cm^{-1}	γ-MnO_2 Raman shift/ cm^{-1}	MnOOH Raman shift/ cm^{-1}
References	69	71	72	73	69	69
746	-	-	-	750	770	625
654	649	640	636	667	658	560
610	-	-	-	538	582	530
575	582	585	574	-	527	494
501	-	515	-	-	494	389
387	392	386	387	-	-	359
296	-	-	-	-	278	285
187	185	184	183.2	-	-	259
138	-	-	-	-	-	148

[a]Assignment of shifts are given in the text.

tunnel can be stabilized by K^+ ions present in the K_2SO_4 supporting electrolyte, which may explain the formation of this crystal phase.[70]

In addition to these peaks, the spectrum exhibits weaker shifts at 138, 301, 501, 610, and 746 cm^{-1}, which do not correspond with bands observed in the α-MnO_2 Raman spectra presented in the literature.[69,71,72] Some of these remaining peaks (138, 301, 501, and 746 cm^{-1}) are present in β-MnO_2,[73] γ-MnO_2, and MnOOH[69] Raman spectra (see Table 1), in addition to peaks in similar positions to that of α-MnO_2, which may lead to some potential overlapping of peaks in the spectra. We postulate the electrodeposited species is therefore predominantly α-MnO_2 with small amounts of β-MnO_2 γ-MnO_2 and unreacted MnOOH consistent with the previously described hydrolysis pathway for the mechanism of the oxidation of manganese dioxide (see eqs 6 and 7).[55]

To attempt to prevent deposition on the electrode, the upscaled experiment was repeated at the lower potential of +0.50 V (vs SCE), that is, corresponding to the onset potential of MnO_2 deposition. The dried carbon particles were analyzed first using SEM/EDX revealing an average weight percent ratio of manganese to carbon of 0.020 ± 0.007 (see Table 1). XPS was used to elucidate the identity of the electrodeposited species. The Mn 2p spectrum is displayed in Figure 6 in which spin−orbit coupling is observed as expected, resulting in a doublet consisting of a $2p_{3/2}$ peak centered at a binding energy of 639.4 eV, which is twice the intensity of the $2p_{1/2}$ peak centered at 650.6 eV. In addition to these two peaks, a small broad feature is observed to the left of the Mn $2p_{3/2}$ and Mn $2p_{1/2}$ peaks at 640.1 and 651.7 eV, respectively, which could indicate the presence of "shake-off" satellite peaks, a feature commonly observed in Mn 2p spectra[74] arising from a core electron being removed completely by photoionization. The assignment of the Mn $2p_{3/2}$ and Mn $2p_{1/2}$ peaks can be somewhat ambiguous due to the small difference in binding energies observed for Mn(III) and Mn(IV).[74−77] For this reason, the deconvolution of the four peaks was conducted for a number of possible scenarios consisting of the sole presence of Mn(III) or Mn(IV) and the combination of these two species with and without the presence of the satellite peaks. The best fit (R_2 = 0.929) was achieved for the presence of Mn(III) and Mn(IV) peaks with satellite peaks (see SI Section E for further Mn 2p XPS spectra and fitting). This is consistent with the MnOOH and MnO_2 species observed previously on the graphite substrate electrode using Raman spectroscopy (Figure 5 and Table 2). Furthermore, the O 1s spectra (Figure

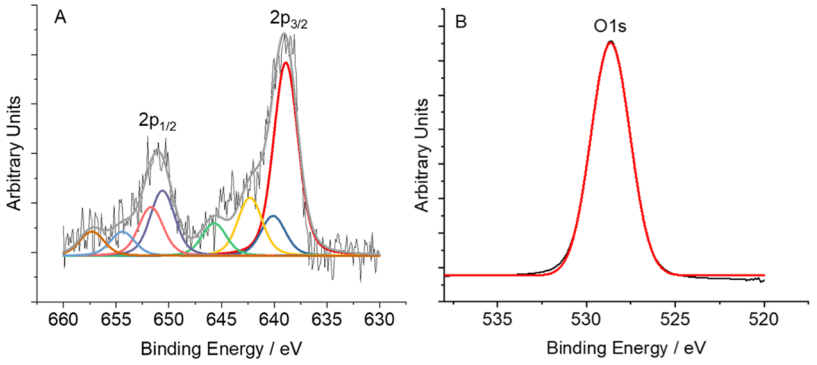

Figure 6. XPS spectra of 0.5 V vs SCE modified CB NP consisting of (A) the high-resolution Mn 2p XPS spectrum with a cumulative peak fit shown in gray. Core-level $2p_{3/2}$ peak fitting for Mn(III) shown in (solid red line) and (solid dark blue line) for Mn(IV) with their corresponding satellite peaks shown in (solid green line) and (solid yellow line), respectively. Core-level $2p_{1/2}$ peak fitting for Mn(III) shown in (solid light blue line) and (solid pink line) for Mn(IV) with their corresponding satellite peaks shown in (solid sky blue line) and (solid brown line) respectively. (B) High-resolution O 1s level with peak fitting shown in (solid red line).

https://doi.org/10.1021/acs.jpcc.3c02964
J. Phys. Chem. C XXXX, XXX, XXX−XXX

6B) exhibit a broad peak centered at a binding energy of 529 eV, which is indicative of O^{2-} present.[77]

CONCLUSIONS

Microelectrode studies and macroelectrode studies on GC indicated that the onset for Mn(II) reduction and oxidation agrees well with the literature. Using impact electrochemistry, Mn(II) reduction and oxidation onto carbon black nanoparticles were demonstrated, where the switch on potential aligns with previously observed onset potentials (−1.44 V vs SCE and +0.5 V vs SCE), respectively. The upscaled impact experiment gave direct evidence for Mn deposition on carbon black shown by SEM/EDX analysis. Lower than expected amounts of MnO_2 were found on the CB NPs, in addition to some intermediate species, which we postulate was due to the mechanism of oxidation of Mn(II). For the development of this method for depositing metals, the use of carbon black particles with a carbon substrate electrode limits the efficiency of deposition/recovery: alternative electrode materials with higher overpotentials for the reduction of the metal of interest should be used to achieve better selectivity in the deposition (i.e., depositing wholly onto the CB particles and not the substrate electrode). Ideally these materials should also have high overpotentials for the hydrogen evolution reaction, and current work is underway to explore the fabrication and use of alternative materials (such as BDD) as microelectrodes for use in this way.

ASSOCIATED CONTENT

Supporting Information

The Supporting Information is available free of charge at https://pubs.acs.org/doi/10.1021/acs.jpcc.3c02964.

Calculations concerning the thermodynamic stability of Mn^{3+} with respect to disproportionation; SEM images and EDX spectra of electrodeposited Mn species on GC electrodes; Mn/MnO_2 coverage calculations; and long-term (5 h) impact chronoamperometry SEM/EDX spectra (PDF)

AUTHOR INFORMATION

Corresponding Author

Neil V. Rees − *School of Chemical Engineering, University of Birmingham, Birmingham B15 2TT, U.K.;* orcid.org/0000-0002-5721-1453; Email: n.rees@bham.ac.uk

Authors

Molly E. Keal − *School of Chemical Engineering, University of Birmingham, Birmingham B15 2TT, U.K.*

James M. Courtney − *Department of Chemical Engineering, Swansea University Bay Campus, Swansea University, Swansea SA1 8EN, U.K.*

Complete contact information is available at: https://pubs.acs.org/10.1021/acs.jpcc.3c02964

Notes

The authors declare no competing financial interest.

ACKNOWLEDGMENTS

The authors wish to thank Dr. Long Jiang (Nanoscale and Microscale Research Centre, University of Nottingham) for assistance in performing XPS measurements and Dr. Kun Zhang (University of Birmingham) for assistance in performing Raman spectroscopy measurements. They also thank The Leverhulme Trust (RPG-2019-146) for funding.

REFERENCES

(1) Botelho, A. B., Jr; de Albuquerque Vicente, A.; Espinosa, D. C. R.; Tenório, J. A. S. Recovery of metals by ion exchange process using chelating resin and sodium dithionite. *J. Mater. Res. Technol.* **2019**, *8*, 4464−4469.

(2) Pohl, A. Removal of Heavy Metal Ions from Water and Wastewaters by Sulfur-Containing Precipitation Agents. *Water Air Soil Pollut.* **2020**, *231*, No. 503.

(3) Tuncuk, A.; Stazi, V.; Akcil, A.; Yazici, E. Y.; Deveci, H. Aqueous metal recovery techniques from e-scrap: Hydrometallurgy in recycling. *Miner. Eng.* **2012**, *25*, 28−37.

(4) Ebin, B.; Isik, M. I. *WEEE Recycling: Research, Development, and Policies*; Elsevier Inc: Amsterdam, 2016; Vol. *5*, pp 139−175.

(5) Jha, M. K.; Lee, J. C.; Kim, M. S.; Jeong, J.; Kim, B. S.; Kumar, V. Hydrometallurgical recovery/recycling of platinum by the leaching of spent catalysts: A review. *Hydrometallurgy* **2013**, *133*, 23−32.

(6) Rai, V.; Tiwari, N.; Rajput, M.; Joshi, S. M.; Nguyen, A. C.; Mathews, N. Reversible Electrochemical Silver Deposition over Large Areas for Smart Windows and Information Display. *Electrochim. Acta* **2017**, *255*, 63−71.

(7) Jin, W.; Hu, M.; Hu, J. Selective and Efficient Electrochemical Recovery of Dilute Copper and Tellurium from Acidic Chloride Solutions. *ACS Sustainable Chem. Eng.* **2018**, *6*, 13378−13384.

(8) Tchounwou, P. B.; Yedjou, C. G.; Patlolla, A. K.; Sutton, DJ. *Heavy Metal Toxicity and the Environment BT - Molecular, Clinical and Environmental Toxicology: Volume 3: Environmental Toxicology*; Luch, A., Ed.; Springer: Basel, 2012; Vol. *101*, pp 133−164.

(9) Oladeji, A. V.; Courtney, J. M.; Rees, N. V. Copper deposition on metallic and non-metallic single particles via impact electrochemistry. *Electrochim. Acta* **2022**, *405*, No. 139838.

(10) Rees, N. V. Electrochemical insight from nanoparticle collisions with electrodes: A mini-review. *Electrochem. Commun.* **2014**, *43*, 83−86.

(11) Robbs, P. H.; Rees, N. V. Nanoparticle electrochemistry. *Phys. Chem. Chem. Phys.* **2016**, *18*, 24812−24819.

(12) Allerston, L. K.; Rees, N. V. Nanoparticle impacts in innovative electrochemistry. *Curr. Opin. Electrochem.* **2018**, *10*, 31−36.

(13) Micka, K. Depolarisation der quecksilbertropfelektrode durch suspensionen unlöslicher stoffe IV. Suspensionen von mangandioxid. *Collect. Czech. Chem. Commun.* **1965**, *30*, 235−245.

(14) Xiao, X.; Fan, F.-R. F.; Zhou, J.; Bard, A. J. Current transients in single nanoparticle collision events. *J. Am. Chem. Soc.* **2008**, *130*, 16669−16677.

(15) Dolinska, J.; Jonsson-Niedziolka, M.; Sashuk, V.; Opallo, M. The effect of electrocatalytic nanoparticle injection on the electrochemical response at a rotating disc electrode. *Electrochem. Commun.* **2013**, *37*, 100−103.

(16) Roberts, J. J. P.; Westgard, J. A.; Cooper, L. M.; Murray, R. W. Solution voltammetry of 4 nm magnetite iron oxide nanoparticles. *J. Am. Chem. Soc.* **2014**, *136*, 10783−10789.

(17) Yoo, J. J.; Kim, J.; Crooks, R. M. Direct electrochemical detection of individual collisions between magnetic microbead/silver nanoparticle conjugates and a magnetized ultramicroelectrode. *Chem. Sci.* **2015**, *6*, 6665−6671.

(18) Zhou, Y. G.; Rees, N. V.; Compton, R. G. The electrochemical detection and characterization of silver nanoparticles in aqueous solution. *Angew. Chem., Int. Ed.* **2011**, *50*, 4219−4221.

(19) Rees, N. V.; Zhou, Y. G.; Compton, R. G. The aggregation of silver nanoparticles in aqueous solution investigated via anodic particle coulometry. *ChemPhysChem* **2011**, *12*, 1645−1647.

(20) Stuart, E. J. E.; Rees, N. V.; Cullen, J. T.; Compton, R. G. Direct electrochemical detection and sizing of silver nanoparticles in seawater media. *Nanoscale* **2013**, *5*, 174−177.

(21) Stuart, E. J. E.; Tschulik, K.; Omanović, D.; Cullen, J. T.; Jurkschat, K.; Crossley, A.; Compton, R. G. Electrochemical detection

of commercial silver nanoparticles: Identification, sizing and detection in environmental media. *Nanotechnology* **2013**, *24*, No. 444002.
(22) Stuart, E. J. E.; Zhou, Y. G.; Rees, N. V.; Compton, R. G. Determining unknown concentrations of nanoparticles: the particle-impact electrochemistry of nickel and silver. *RSC Adv.* **2012**, *2*, 6879−6884.
(23) Batchelor-Mcauley, C.; Ellison, J.; Tschulik, K.; Hurst, P. L.; Boldt, R.; Compton, R. G. In situ nanoparticle sizing with zeptomole sensitivity. *Analyst* **2015**, *140*, 5048−5054.
(24) Haddou, B.; Rees, N. V.; Compton, R. G. Nanoparticle-electrode impacts: The oxidation of copper nanoparticles has slow kinetics. *Phys. Chem. Chem. Phys.* **2012**, *14*, 13612−13617.
(25) Zhou, Y. G.; Rees, N. V.; Compton, R. G. Electrochemistry of nickel nanoparticles is controlled by surface oxide layers. *Phys. Chem. Chem. Phys.* **2013**, *15*, 761−763.
(26) Zhong, R.; Wang, X.; Tao, Q.; Zhang, J.; Lin, C.; Wei, H.; Zhou, Y.-G. From Ensemble Electrochemistry to Nano-Impact Electrochemistry: Altered Reaction Selectivity. *Angew. Chem., Int. Ed.* **2022**, *61*, No. e202207270.
(27) Zhang, W.; Li, J.; Xia, X.-H.; Zhou, Y.-G. Enhanced Electrochemistry of Single Plasmonic Nanoparticles. *Angew. Chem., Int. Ed.* **2022**, *61*, No. e202115819.
(28) Kumar, A. K. S.; Compton, R. G. Understanding Carbon Nanotube Voltammetry: Distinguishing Adsorptive and Thin Layer Effects via "Single-Entity" Electrochemistry. *J. Phys. Chem. Lett.* **2022**, *13*, 5557−5562.
(29) Kumar, A. K. S.; Compton, R. G. Single-Entity "Nano-Catalysis": Carbon Nanotubes and the VO2+/VO2+ Redox Reaction. *ACS Catal.* **2022**, *12*, 4754−4764.
(30) Zampardi, G.; Compton, R. G. Fast electrodeposition of zinc onto single zinc nanoparticles. *J. Solid State Electrochem.* **2020**, *24*, 2695−2702.
(31) Zhou, Y. G.; Rees, N. V.; Compton, R. G. Nanoparticle-electrode collision processes: The underpotential deposition of thallium on silver nanoparticles in aqueous solution. *ChemPhysChem* **2011**, *12*, 2085−2087.
(32) Zhou, Y. G.; Rees, N. V.; Compton, R. G. Nanoparticle-electrode collision processes: The electroplating of bulk cadmium on impacting silver nanoparticles. *Chem. Phys. Lett.* **2011**, *511*, 183−186.
(33) Oladeji, A. V.; Courtney, J. M.; Fernandez-Villamarin, M.; Rees, N. V. Electrochemical Metal Recycling: Recovery of Palladium from Solution and In Situ Fabrication of Palladium-Carbon Catalysts via Impact Electrochemistry. *J. Am. Chem. Soc.* **2022**, *144*, 18562−18574.
(34) Li, H.; Zhang, X.; Sun, Z.; Ma, W. Rapid Screening of Bimetallic Electrocatalysts Using Single Nanoparticle Collision Electrochemistry. *J. Am. Chem. Soc.* **2022**, *144*, 16480−16489.
(35) Gong, J.; Wei, G.; Barnard, J. A.; Zangari, G. Electrodeposition and Characterization of Sacrificial Copper-Manganese Alloy Coatings: Part II. Structural, Mechanical, and Corrosion-Resistance Properties. *Metall. Mater. Trans. A* **2005**, *36*, 2705−2715.
(36) Agency for Toxic Substances and Disease Registry 2022 https://wwwn.cdc.gov/TSP/PHS/PHS.aspx?phsid=100&toxid=23. (accessed: October 2022).
(37) Blanc, P. D. The early history of manganese and the recognition of its neurotoxicity. *Neurotoxicology* **2018**, *64*, 5−11.
(38) Buzatu, T.; Popescu, G.; Birloaga, I.; Sa, S. Study concerning the recovery of zinc and manganese from spent batteries by hydrometallurgical processes. *Waste Manage.* **2013**, *33*, 699−705.
(39) Dwivedi, D.; Randhawa, N. S.; Saroj, S.; Jana, R. K. An Overview of Manganese Recovery by Hydro and Pyro-Metallurgical Routes. *J. Inst. Eng. (India): Ser. D* **2017**, *98*, 147−154.
(40) Smith, Y. R.; Nagel, J. R.; Rajamani, R. K. Eddy current separation for recovery of non-ferrous metallic particles: A comprehensive review. *Miner. Eng.* **2019**, *133*, 149−159.
(41) Allmand, A.; Campbell, A. N. The electrodeposition of manganese − Part I. *Trans. Faraday Soc.* **1924**, *19*, 559−570.
(42) Gonsalves, M.; Pletcher, D. A study of the electrodeposition chloride electrolytes of manganese from aqueous. *J. Electroanal. Chem. Interfacial Electrochem.* **1990**, *285*, 185−193.
(43) Lewis, J. E.; Scaife, P. H.; Swinkels, D. A. J. Electrolytic manganese metal from chloride electrolytes. I. Study of deposition conditions. *J. Appl. Electrochem.* **1976**, *6*, 199−209.
(44) Fernández-barcia, M.; Hoffmann, V.; Oswald, S.; Wolff, U.; Uhlemann, M.; Gebert, A. Electrodeposition of manganese layers from sustainable sulfate based electrolytes. *Surf. Coat. Technol.* **2008**, *334*, 261−268.
(45) Oaks, H. H.; Bradt, W. E. The Electrodeposition of Manganese from Aqueous Solutions: I. chloride electrolytes. *Trans. Electrochem. Soc.* **1936**, *69*, No. 567.
(46) Bradt, W. E.; Taylor, L. R. The Electrodeposition of Manganese from Aqueous Solutions: II. sulfate electrolytes. *Trans. Electrochem. Soc.* **1937**, *73*, No. 327.
(47) Gong, J.; Zangari, G. Electrodeposition and Characterization of Manganese Coatings. *J. Electrochem. Soc.* **2002**, *149*, No. C209.
(48) Gong, J.; Zana, I.; Zangari, G. Electrochemical synthesis of crystalline and amorphous manganese coatings. *J. Mater. Sci. Lett.* **2001**, *20*, 1921−1923.
(49) Jiao, P.; Xu, F.; Li, J.; Duan, N.; Chen, G.; Jiang, L. The inhibition effect of SeO_2 on hydrogen evolution reaction in MnSO4−(NH4)2SO4 solution. *Int. J. Hydrogen Energy* **2016**, *41*, 784−791.
(50) Lu, J.; Dreisinger, D.; Glück, T. Manganese electrodeposition — A literature review. *Hydrometallurgy* **2014**, *141*, 105−116.
(51) Yanitskii, I. V.; Suliakas, A.; Stul'Pinas, B. B. The effect of H_2SeO_3 on the electrodeposition of Mn. *Tr. Akad. Nauk Lit. SSR, Ser. B* **1961**, 107−118.
(52) Goddard, J. B.; Hansen, D. J. Method for electrolytic deposition of manganese. U.S. Patent US4149944A, 1977.
(53) Batchelor-McAuley, C. Defining the Onset Potential. *Curr. Opin. Electrochem.* **2022**, *37*, No. 101176.
(54) Ding, K. Q. Direct Preparation of Metal Ions-doped Manganese Oxide by Cyclic Voltammetry. *J. Chin. Chem. Soc.* **2008**, *55*, 543−549.
(55) Clarke, C. J.; Browning, G. J.; Donne, S. W. An RDE and RRDE study into the electrodeposition of manganese dioxide. *Electrochim. Acta* **2006**, *51*, 5773−5784.
(56) Paul, R. L.; Cartwright, A. The mechanism of the deposition of manganese dioxide. *J. Electroanal. Chem. Interfacial Electrochem.* **1986**, *201*, 123−131.
(57) Paul, R. L.; Cartwright, A. The mechanism of the deposition of manganese dioxide. Part II. Electrode impedance studies. *J. Electroanal. Chem. Interfacial Electrochem.* **1986**, *201*, 113−122.
(58) Comninellis, C.; Petitpierre, J. P. Electrochemical oxidation of Mn(II) to MnO_4^- in the presence of Ag(I) catalyst. *Electrochim. Acta* **1991**, *36*, 1363−1365.
(59) Das, D.; Sen, P. K.; Das, K. Mechanism of potentiostatic deposition of MnO_2 and electrochemical characteristics of the deposit in relation to carbohydrate oxidation. *Electrochim. Acta* **2008**, *54*, 289−295.
(60) Ghaemi, M.; Khosravi-Fard, L.; Neshati, J. Improved performance of rechargeable alkaline batteries via surfactant-mediated electrosynthesis of MnO2. *J. Power Sources* **2005**, *141*, 340−350.
(61) Kätelhön, E.; Tanner, E. E. L.; Batchelor-Mcauley, C.; Compton, R. G. Destructive nano-impacts: What information can be extracted from spike shapes? *Electrochim. Acta* **2016**, *199*, 297−304.
(62) Navrotsky, A. Nanoscale Effects on Thermodynamics and Phase Equilibria in Oxide Systems. *ChemPhysChem* **2011**, *12*, 2207−2215.
(63) Navrotsky, A.; Ma, C.; Lilova, K.; Birkner, N. Nanophase Transition Metal Oxides Show Large Thermodynamically Driven Shifts in Oxidation-Reduction Equilibria. *Science* **2010**, *330*, 199−201.
(64) Sun, W.; Kitchaev, D. A.; Kramer, D.; Ceder, G. Non-equilibrium crystallization pathways of manganese oxides in aqueous solution. *Nat. Commun.* **2019**, *10*, No. 573.
(65) Chen, B.-R.; Sun, W.; Kitchaev, D. A.; Mangum, J. S.; Thampy, V.; Garten, L. M.; Ginley, D. S.; Gorman, B. P.; Stone, K. H.; Ceder, G.; et al. Understanding crystallization pathways leading to manganese oxide polymorph formation. *Nat. Commun.* **2018**, *9*, No. 2553.

https://doi.org/10.1021/acs.jpcc.3c02964
J. Phys. Chem. C XXXX, XXX, XXX−XXX

(66) Kitchaev, D. A.; Dacek, S. T.; Sun, W.; Ceder, G. Thermodynamics of Phase Selection in MnO2 Framework Structures through Alkali Intercalation and Hydration. *J. Am. Chem. Soc.* **2017**, *139*, 2672−2681.
(67) Ma, H.; Chen, J. F.; Wang, H. F.; Hu, P. J.; Ma, W.; Long, Y. T. Exploring dynamic interactions of single nanoparticles at interfaces for surface-confined electrochemical behavior and size measurement. *Nat. Commun.* **2020**, *11*, No. 2307.
(68) Fu, J.; Luo, X. A first-principles investigation of α, β, and γ-MnO_2 as potential cathode materials in Al-ion batteries. *RSC Adv.* **2020**, *10*, 39895−39900.
(69) Sun, M.; Lan, B.; Lin, T.; Cheng, G.; Ye, F.; Yu, L.; et al. Controlled synthesis of nanostructured manganese oxide: Crystalline evolution and catalytic activities. *CrystEngComm* **2013**, *15*, 7010−7018.
(70) Duan, X.; Yang, J.; Gao, H.; Ma, J.; Jiao, L.; Zheng, W. Controllable hydrothermal synthesis of manganese dioxide nanostructures: Shape evolution, growth mechanism and electrochemical properties. *CrystEngComm* **2012**, *14*, 4196−4204.
(71) Zhang, B.; Cheng, G.; Lan, B.; Zheng, X.; Sun, M.; Ye, F.; et al. Crystallization design of MnO_2: Via acid towards better oxygen reduction activity. *CrystEngComm* **2016**, *18*, 6895−6902.
(72) Revathi, C.; Kumar, R. T. R. Electro Catalytic Properties of α, β, γ, ϵ - MnO_2 and γ - MnOOH Nanoparticles: Role of Polymorphs on Enzyme Free H_2O_2 Sensing. *Electroanalysis* **2017**, *29*, 1481−1489.
(73) Gao, T.; Fjellvåg, H.; Norby, P. A comparison study on Raman scattering properties of α- and β-MnO_2. *Anal. Chim. Acta* **2009**, *648*, 235−239.
(74) Amano, M. E.; Betancourt, I.; Arellano-Jimenez, M. J.; Sánchez-Llamazares, J. L.; Sánchez-Valdés, C. F. Magnetocaloric response of submicron (LaAg)MnO_3 manganite obtained by Pechini method. *J. Sol-Gel Sci. Technol.* **2016**, *78*, 159−165.
(75) Bao, B.; Liu, J.; Xu, H.; Liu, B.; Zhang, K.; Jin, Z. Insight into a high temperature selective oxidation of HP_40 alloy under a H_2−H_2O environment. *RSC Adv.* **2017**, *7*, 8589−8597.
(76) Wang, Y.; Guan, H.; Du, S.; Wang, Y. A facile hydrothermal synthesis of MnO_2 nanorod-reduced graphene oxide nanocomposites possessing excellent microwave absorption properties. *RSC Adv.* **2015**, *5*, 88979−88988.
(77) Stranick, M. A. MnO_2 by XPS. *Surf. Sci. Spectra* **2021**, *6*, 31−38.

https://doi.org/10.1021/acs.jpcc.3c02964
J. Phys. Chem. C XXXX, XXX, XXX−XXX